Seeded and unseeded helical modes in magnetized, non-imploding cylindrical liner-plasmas

D. A. Yager-Elorriaga,[a] P. Zhang, A. M. Steiner, N. M. Jordan, Y. Y. Lau, and R. M. Gilgenbach
Department of Nuclear Engineering and Radiological Sciences, University of Michigan, Ann Arbor, Michigan 48109-2104, USA

In this research, we generated helical instability modes using unseeded and kink-seeded, non-imploding liner-plasmas at the 1 MA Linear Transformer Driver facility at the University of Michigan in order to determine the effects of externally applied, axial magnetic fields. In order to minimize the coupling of sausage and helical modes to the magneto Rayleigh-Taylor instability, the 400 nm-thick aluminum liners were placed directly around straight-cylindrical (unseeded) or threaded-cylindrical (kink-seeded) support structures to prevent implosion. The evolution of the instabilities was imaged using a combination of laser shadowgraphy and visible self-emission, collected by a 12-frame fast intensified CCD camera. With no axial magnetic field, the unseeded liners developed an azimuthally correlated $m = 0$ sausage instability (m is the azimuthal mode number). Applying a small external axial magnetic field of 1.1 T (compared to peak azimuthal field of 30 T) generated a smaller amplitude, helically oriented instability structure that is interpreted as an $m = +2$ helical mode. The kink-seeded liners showed highly developed helical structures growing at the seeded wavelength of $\lambda = 1.27$ mm. It was found that the direction of the axial magnetic field played an important role in determining the overall stabilization effects; modes with helices spiraling in the opposite direction of the global magnetic field showed the strongest stabilization. Finally, the Weis-Zhang analytic theory [Weis *et al.*, Phys. Plasmas **22**, 032706 (2015)] is used to calculate sausage and helical growth rates for experimental parameters in order to study the effects of axial magnetic fields. *Published by AIP Publishing.* [http://dx.doi.org/10.1063/1.4965240]

I. INTRODUCTION

A fast Z-pinch may be created by driving a large axial current through a conductor, so that the self-generated Lorentz force implodes the system to high energy density conditions; a process that is generally accompanied by the production of x-ray radiation. The geometry of such systems tends to be cylindrical, for example, in gas puff Z-pinches,[1,2] cylindrical wire arrays,[3–5] and magnetized target fusion schemes,[6–8] which means that the magneto Rayleigh-Taylor (MRT) instability of an accelerating interface may couple to the traditional sausage and kink instabilities of a current carrying column.[9,10] These instabilities limit the fusion neutron yield and x-ray radiation via non-uniform implosions and poor confinement, motivating the study and mitigation of these processes. One particular mitigation technique is through the use of axial magnetic fields, where axisymmetric structures must bend magnetic field lines in order to grow.

Studies of MRT on the Z Machine at Sandia National Laboratories using unseeded, imploding cylindrical liners without axial magnetic fields have found instability structures that align themselves along roughly horizontal planes.[11] In this fashion, the interchange of the magnetic field and plasma minimizes magnetic field line bending, favoring the axisymmetric structure. However, the inclusion of a relatively weak axial magnetic field of 7 T shifted these structures to a helical shape[12] despite the puzzling fact that these structures must bend the large azimuthal magnetic field (>1000 T). University-scale experiments of non-imploding liners have similarly found azimuthally correlated structures when no axial magnetic field is present, and helically oriented structures when an axial magnetic field is applied.[13,14] One possible interpretation of these results is that the helical structure arises due to non-axisymmetric modes (such as the kink instability) that have been seeded early on when the bulk liner motion is small (so that MRT is negligible), and the axial magnetic field is large compared to the azimuthal field.[9,10] The persistence of the helical feature,[12] despite the subsequent rapid increase and dominance of the azimuthal magnetic field, was demonstrated to be a manifestation of such a discrete non-axisymmetric eigenmode.[9]

The purpose of this paper is to explore the dominance and stabilization of helical structures that appear in the presence of axial magnetic fields. In order to minimize liner acceleration and MRT effects, we have developed two types of cylindrical liner loads to study the onset and development of sausage and helical instabilities, driven by the 1 MA Linear Transformer Driver (LTD) at the University of Michigan.[15] In this paper, we label the MRT effect as the instability mechanism due only to acceleration of the liner, separate from the traditional sausage and kink instabilities; the latter do not require liner acceleration. The first type of liner consists of an ultrathin (400 nm-thick) aluminum foil wrapped directly around a 6.35 mm diameter plastic rod in

[a]Electronic mail: dyager@umich.edu

TABLE I. Summary of experimental configuration and results. Two values are used for the shot 1189 growth rate data, corresponding to the two distinct regions of growth due to the change in wavelength from the merging of instability bumps.

Shot	Load	Axial B field (T)	Azimuthal mode	Growth rate (μm/ns)	Expansion rate (μm/ns)	Image timing (ns)
1189	Unseeded	0	$m = 0$	1.8 ± 0.2, 2.7 ± 0.4	3.8 ± 0.2	246–346
1190	Unseeded	$+1.1$	$m = +2$	1.6 ± 0.1	3.6 ± 0.1	254–354
1192	Kink–seeded	0	$m = 1$	2.2 ± 0.2	5.2 ± 0.3	192–292
1205	Kink-seeded	-1.6	$m = +1$	3.5 ± 0.2	5.5 ± 0.5	204–304
1193	Kink-seeded	$+1.6$	$m = -1$	1.4 ± 0.3	4.6 ± 0.3	225–325

order to prohibit the liner from imploding. For the second type of liner, the support rod is modified using a helically threaded plastic screw in order to seed the $m = +1$ kink mode (m is the azimuthal mode number, defined in Sec. II with respect to the global magnetic field). Using 12-frame laser shadowgraphy and visible self-emission, we have found that the unseeded liner developed an azimuthally symmetric $m = 0$ sausage mode, and that in the presence of a relatively small axial magnetic field of 1.1 T (compared to the peak azimuthal field of 30 T), helically oriented instability structures arose, with an overall reduced amplitude, which are interpreted as an $m = +2$ helical mode. For the kink-seeded liners, we have found that the axial magnetic field significantly reduced the instability growth *only when the direction of the seeded spiral was in the opposite direction of the global magnetic field spiral.*

II. THEORETICAL BACKGROUND

The traditional sausage and kink instabilities arise from perturbations of the form $\exp(im\theta - i2\pi z/\lambda)$, where m is the azimuthal mode number (which may be positive, negative, or zero) and λ is the axial wavelength of the instability. The axisymmetric $m = 0$ mode and the helically oriented $|m| = 1$ mode are commonly referred to as the sausage and kink modes, respectively. For the $|m| = 1$ mode, an azimuthal variation of 2π traces a constant perturbation a distance of one axial wavelength, resulting in a single helical structure. For $|m| > 1$, an azimuthal variation of 2π traces a constant perturbation at distance of $|m|$ axial wavelengths, resulting in a structure consisting of $|m|$ intertwined helices. In this paper, all $|m| \geq 1$ modes shall collectively be referred to as helical modes, with the following sign convention for the azimuthal mode number, m. A helix observed in the experimental images in Fig. 5 is assigned a positive (negative) azimuthal mode number $+m$ $(-m)$ if this helix is in the same (opposite) sense of rotation as the global magnetic field, which has a nonzero axial magnetic field B_z in addition to azimuthal magnetic field B_θ. Note that for the positive m mode, the plasma helix need not be perfectly aligned with the global magnetic field. A helical mode with no sign attached to the azimuthal mode number (m) shall be used to indicate that there is no axial magnetic field. This sign convention is used in Table I for the azimuthal mode number. In this convention, the $-m$ modes tend to be more stable than the $+m$ modes because the former have a higher degree of magnetic field line bending, a well-known stabilizing influence for MHD modes. Figure 1 shows physical representation of the $m = 0$, $m = \pm1$, and $m = +2$ modes.

In an imploding cylindrical liner, sausage and helical modes may couple to the magneto Rayleigh-Taylor instability when the liner undergoes radial acceleration. The general dispersion relation for this scenario was calculated analytically by Weis and Zhang for an arbitrary axial magnetic field using linear perturbation theory, ideal MHD, and a sharp boundary model.[9,10] The Weis-Zhang theory has been qualitatively used to describe the evolution of instability development in MagLIF liners[9] and shall be used to interpret the experimental results in this paper by setting the interface acceleration to zero in Section V B. While the experimental data for this paper were taken at a time when the instabilities have grossly developed (likely beyond the direct applicability of perturbation theory), the Weis-Zhang theory may still be used to (1) understand instability development that has occurred earlier in time when the instability amplitudes were small and, in particular, to (2) determine the effects of axial magnetic fields on the various m-modes.
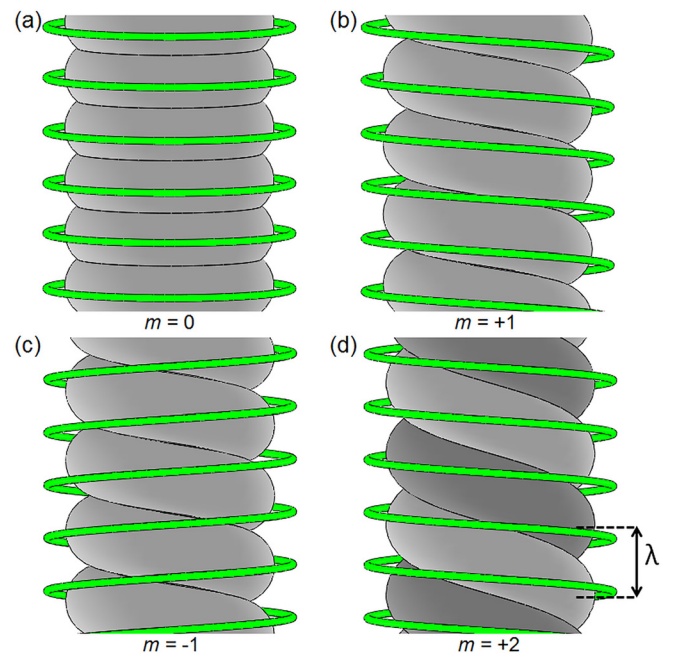

FIG. 1. Physical picture of instability structures with azimuthal mode number (a) $m = 0$, (b) $m = +1$, (c) $m = -1$, and (d) $m = +2$. Also shown is the axial wavelength λ, defined as the distance between adjacent instability structures. The global magnetic field is represented by the thin green line. A positive m (negative m) mode indicates the plasma helix rotates in the same (opposite) sense as the global magnetic field. The $m = +1$ and the $m = -1$ mode consist of a single helix, whereas the $m = +2$ mode consists of two intertwined helices (shown as dark and light in (d)). Note that in (d), when the light (or dark) helix traces an azimuthal angle of 2π, the axial distance advances by 2λ.

III. EXPERIMENTAL CONFIGURATION

The experiments were performed at the Michigan Accelerator for Inductive Z-Pinch Experiments (MAIZE) facility at the University of Michigan, using a 1-MA Linear Transformer Driver (LTD).[15] The two types of non-imploding targets used were *unseeded* and *kink-seeded* ultrathin liners, fabricated using a technique similar to Ref. 16. For this experiment, the targets were fabricated by directly wrapping the foil around an unmodified straight-cylindrical or threaded-cylindrical (1/4″-20 imperial) plastic rod. The experimental configuration and support structures are shown in Fig. 2. The unseeded support structure had a diameter of 6.35 mm, and the screw-seeded support structure had a mean diameter of 5.65 mm with 0.8 mm peak-to-valley amplitude and 1.27 mm axial wavelength. For the seeded support structure, the initial spiral impression on the foil was negligible as the foil made minimal contact with the edges of the screw threads. During the discharge, the foil ablates and plasma fills the gaps, taking the shape of the screw pattern and therefore seeding the kink instability. The MRT development during this process is expected to be minimal (see Section V A). Due to the inductive nature of the targets, the peak current was approximately 570 kA with 165 ns 10%–90% risetime (see Fig. 3) and was approximately equal for the five shots presented in this paper. Therefore, the overall magnetic field, and thus the driving force for the sausage and helical instabilities, was

FIG. 3. LTD current traces and image timings. Each shot consisted of 11 images over 100 ns with 10 ns interframe delay. The timings of the first and last frame are marked by each symbol.

approximately equal, which means these shots may be directly compared.

The plasmas were magnetized using a set of Helmholtz Coils[17] driven by a separate 1.2 mF capacitor bank. The axial magnetic field peaked in 2 ms, which allowed the field to fully diffuse through the hardware and pre-magnetize the liner. The field diffusion was studied using the transient magnetic field solver in Ansys Maxwell and directly measured with a fast Hall-effect magnetic field probe along the liner axis. The Hall probe was used to calibrate a separate B-dot probe located on the top of the coil housing, which measured the axial magnetic field for an individual shot. Limited by our capacitor bank, the coils are capable of producing fields up to 5.5 T; however, axial fields of 1.1 T and 1.6 T were used for this experiment to reduce the mechanical strain on the coils.

The plasmas were imaged using a combination of shadowgraphy and self-emission, collected by a 12-frame intensified CCD camera, gated at 10 ns for this experiment. The imaging laser used in these experiments was a 532 nm, 2 ns pulse length, frequency-doubled Nd:YAG laser. The shadowgraphy system is shown in Fig. 4, which employed a 3.05 m resonating cavity with two 95%/5% beam splitters, corresponding to a 10 ns delay between pulses. The first beam splitter allowed the laser pulse to enter the cavity, and the second beam splitter directed the train of pulses through the target chamber and to the imaging system. Due to the two beam splitters, the intensity of each subsequent pulse is
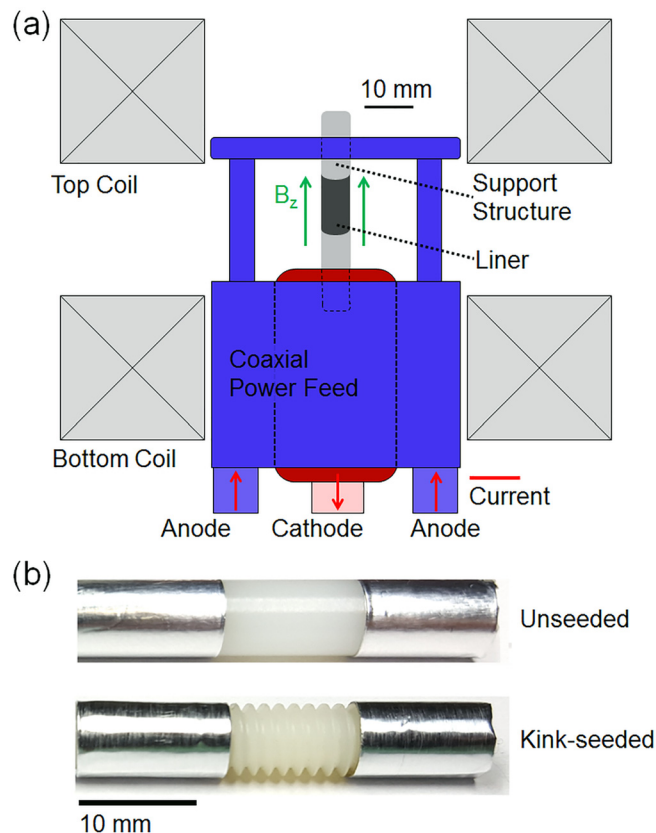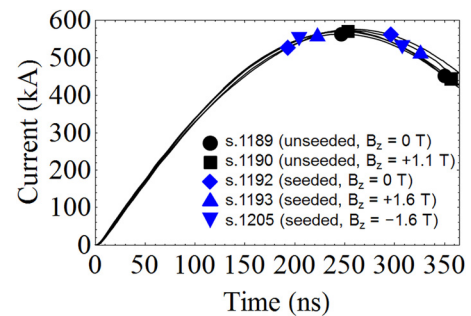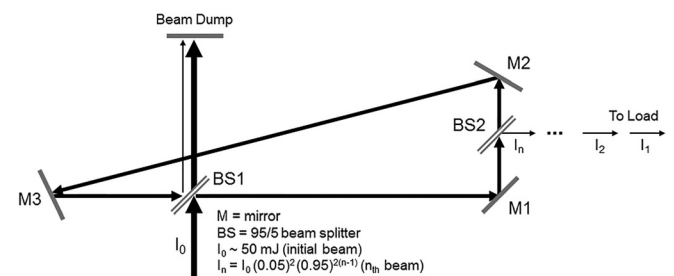

FIG. 2. (a) Schematic of load hardware configuration and (b) image of unseeded and kink-seeded liner support structures. The 400 nm aluminum foil is wrapped directly around the non-conducting region so that contact is made on the conducting ends.

FIG. 4. Optical system used to generate 12+ superimposed beams (not drawn to scale). The incident pulse (2 ns pulse length, 532 nm wavelength, ~50 mJ) is passed through beam splitter BS1 so that a small fraction of the beam is trapped between the resonating cavity formed by mirrors M1, M2, and M3. Beam splitter BS2 directs a sequence of pulses to the target chamber. The 2 ns length pulses are delayed temporally by 10 ns due to the 3.05 m resonating cavity length.

reduced by ∼10%. The framing camera collected the 2 ns backlit image in addition to plasma self-emission (filtered at 532 nm) over the 10 ns framing-camera window. This system allowed the tracking of individual features from the same angle of incidence in both shadowgraphy and self-emission with 12-frames over a 110 ns window.

IV. EXPERIMENTAL RESULTS

Five shots consisting of 55 shadowgraph/self-emission images in total were obtained for this campaign and are summarized in Table I. The current traces (Fig. 3) agreed within 2% at peak current (250 ns) and 9% at the end of the pulse (350 ns). A selection of images is shown in Fig. 5, where the
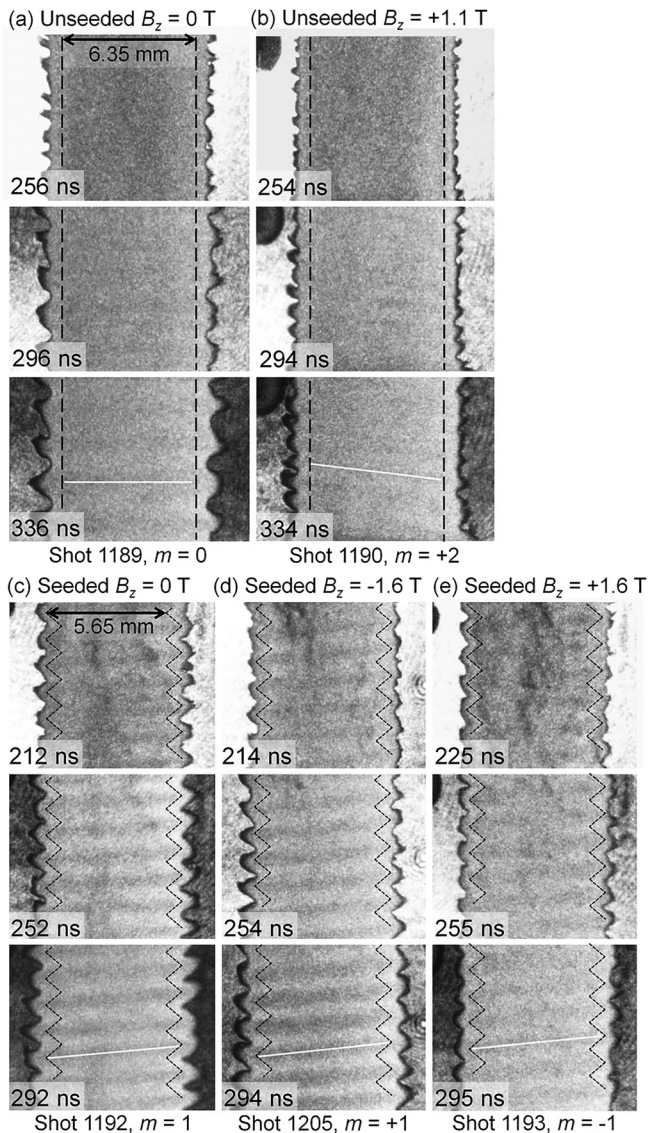

FIG. 5. A selection of shadowgraphy/self-emission images comparing instability development and self-emission structures for: (a) unseeded, unmagnetized liner, (b) unseeded, magnetized liner (+1.1 T), (c) kink-seeded, unmagnetized liner, (d) kink-seeded, magnetized liner (−1.6 T), and (e) kink-seeded, magnetized liner (+1.6 T). The shot number and azimuthal mode m are listed below the images. The approximate position of the support structures and sample self-emission striations are outlined in black and white, respectively. The current is in the −**z** direction. Images filtered at 532 nm; brightness corresponds to incident energy on camera.

approximate position of the support structures is marked as the dashed black line, and sample self-emission striation lines are marked in white (last frame only). The images showed instability structures forming on the edge of the liners, outlined by a thin dark band due to shadowgraphy, and dark and bright striations in self-emission that connected the instability bumps and necks across the plasma, respectively. This series of shots used a small screw (#2–52 imperial) as a fiducial, located near the top of the plasma (the fiducial was placed farther away for shot 1189). A lower density plasma formed on the fiducial screw and expanded towards the liner-plasma; however, the perturbation on the instability structures was small.

The unseeded, unmagnetized liner images show azimuthally correlated instability structures that grew in amplitude. As the interface acceleration was minimal, these azimuthally correlated structures are attributed to the current-driven, axisymmetric $m = 0$ sausage instability. At 290 ns, the smaller axial wavelength structures ($\lambda = 0.9$ mm) merged into longer wavelength structures ($\lambda = 1.7$ mm, Fig. 5(a)), retaining their axisymmetric nature throughout the merging process. After this time, the longer wavelength structures continued to grow in amplitude.

Adding a relatively small axial magnetic field of 1.1 T in the +z direction (compared to the peak azimuthal field of 30 T) destroyed the azimuthal symmetry and resulted in both smaller amplitude instability bumps and helically oriented self-emission striations (Fig. 5(b)) with similar wavelengths (0.8 mm) to the smaller structures of the unmagnetized liner. The self-emission features were much fainter than the unmagnetized case, which may be attributed to the smaller amplitude of the instability structures. A contrast-enhanced, false color image of an unseeded, magnetized liner is shown in Fig. 6 and analyzed in Section V A.

The kink-seeded liners developed helical instability structures at the seeded axial wavelength of $\lambda = 1.27$ mm, regardless of the magnetic field orientation. This indicates that the helical shape of the support structure was the dominant factor for determining the physical structure of instability, superseding the global magnetic field orientation. However, the axial magnetic field orientation did affect the
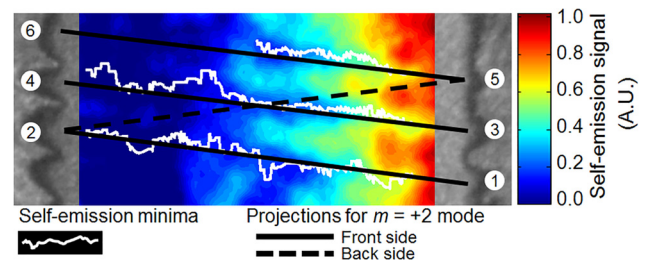

FIG. 6. Analysis of azimuthal mode number for unseeded, $B_z = +1.1$ T magnetized liner (shot 1190). The central region has been contrast-enhanced. White lines correspond to dark striations, measured using an algorithm that tracks self-emission minima. Superimposed on the figure are the required bump-to-bump striations for an $m = +2$ helical mode. For the measured striation angles on the back side of plasma to be conserved from the front side, bump #2 must connect to bump #5, agreeing with the superimposed $m = +2$ mode. The figure may also be used to show that the interpretation of an $m = +1$ mode is unreasonable: bump #2 would connect to bump #3, implying a striation angle of zero degrees on the backside.

amplitude of the instabilities; an axial field of 1.6 T in the –**z** direction did not significantly change the amplitude of the structures (Fig. 5(d)) when compared to the unmagnetized case (Fig. 5(c)), whereas reversing the direction of the field *did* have a significant effect, resulting in a peak instability amplitude of nearly half the value (Fig. 5(e)). The helix in Fig. 5(e), being a negative azimuthal mode, invokes more magnetic field bending and therefore reduces growth in amplitude. In general, the bright and dark self-emission striations demonstrated a higher contrast when compared to the unseeded liners; the striations for the $B_z = 0$ and $B_z = -1.6$ T liners were particularly clear (Figs. 5(c) and 5(d)), which may be attributed to their larger instability amplitudes when compared to the $B_z = +1.6$ T liner.

In order to quantify these results, the vacuum-plasma boundary was traced. The sharpness of the dark line outlining the plasma permitted manual tracking of the plasma boundary, which was taken to be the outermost black edge of the shadowgraphy features. A more rigorous method could use an algorithm to track the boundary; however, the clarity of the black line indicated that the tracings were not unduly subjective. For left and right sides, the radius of the plasma was taken to be the mean position of the tracing, and the centerline of the plasma was taken to be the average of the left and right radii of the first frame. The instability amplitude A was characterized by the standard deviation σ in the radial position of the tracings using the amplitude relation for a perfect sine wave, $A = \sqrt{2}\sigma$. In this manner, the radius and instability amplitude could be determined as a function of time by taking the mean of the left and right values, with uncertainties estimated using the difference between the left and right measurements. These results are presented in Fig. 7.

V. ANALYSIS AND DISCUSSION

A. Analysis of experimental results

The experimental data show that an axial magnetic field reduces overall instability growth, for both seeded and unseeded configurations (Figs. 7(a) and 7(b)). The amplitude tended to grow algebraically (as opposed to exponentially), which indicates that the observed growth had reached the nonlinear regime. The algebraic growth rate could be quantified by fitting a linear regression to the linearly increasing regions of the amplitude in Figs. 7(a) and 7(b). The data for the unseeded, unmagnetized liner were split into two regions as shown in Fig. 7(a), corresponding to (1) the instability wavelength of $\lambda = 0.9$ mm ($t < 290$ ns) and (2) the merged wavelength of $\lambda = 1.6$ mm ($t > 290$ ns). The measured growth rates are summarized in Table I, where uncertainties are estimated using the standard error of the linear regression. Interestingly, the growth rate for the longer wavelength structure of the unseeded, unmagnetized liner increased ($t > 290$ ns, Fig. 7(a)), whereas perturbation theory predicts a decrease.[9,10] A possible mechanism is this: between 240 and 290 ns, the short wavelength $m = 0$ sausage mode has already reached the nonlinear state, during which the instability undergoes algebraic growth, which is much milder than the likely exponential growth that occurred earlier (but was not
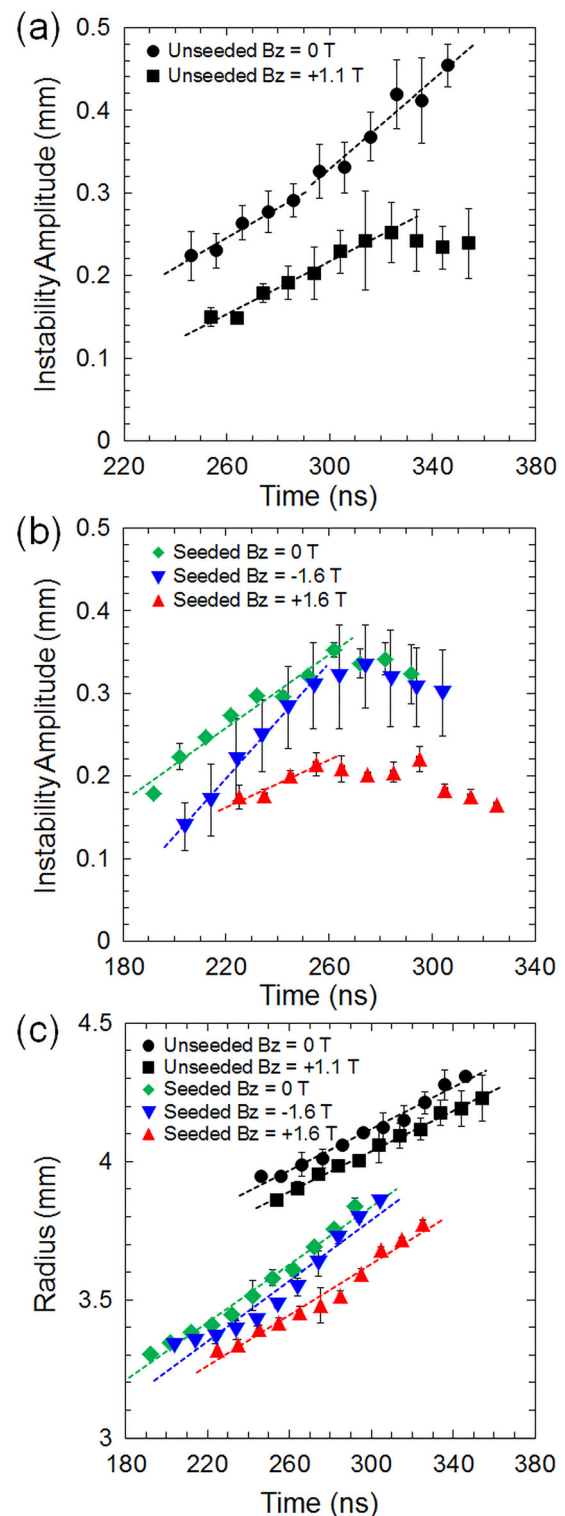

FIG. 7. Experimental data for (a) unseeded instability amplitude, (b) seeded instability amplitude, and (c) mean plasma radius. The linear fits to the amplitude and radius are summarized in Table I. To best characterize the growth rate, only the linear regions of amplitude were fit, and the unseeded, unmagnetized data were separated into two regions, corresponding to the initial ($t < 290$ ns) and merged ($t > 290$ ns) instability structures.

imaged) when perturbation theory was applicable. Around 290 ns, merging of bumps occurs, and the axial wavelength is thus increased substantially, making the amplitude of the perturbation much smaller than the (merged) axial wavelength in comparison. This makes the perturbation theory

applicable again because of the "small" amplitude of the perturbation with respect to the instability wavelength, thus leading to the stronger (exponential) growth beyond 290 ns, as suggested in the "Unseeded $B_z = 0$ T" data in Fig. 7(a). It is interesting to note that *every* small wavelength structure merged with an adjacent pair in order to create a coherent, longer wavelength, azimuthally correlated structure. For the kink-seeded data in Fig. 7(b), the $B_z = 0$ and $B_z = -1.6$ T liners had instability structures that grew to nearly equal amplitudes at 270 ns. Before this time, however, the $B_z = -1.6$ T liner showed a reduction in instability amplitude. On the other hand, the $B_z = +1.6$ T liner showed the smallest instability structures overall, along with a saturation in growth beginning at 260 ns. An explanation for these results is presented later in the paper.

During the imaging window, the plasma expanded throughout the discharge with an approximately constant velocity, as indicated by the plot of mean radius versus time, given in Fig. 7(c). For each shot, the entire dataset was fit using a linear regression with uncertainties estimated by the standard error; these results are summarized in Table I and indicate that the plasma-vacuum interface acceleration, and therefore MRT growth, was likely to be small. The constant-velocity expansion assumption may be limited when considering the $B_z = -1.6$ T seeded liner, which underwent the most complex radial expansion. During the majority of the imaging period, the mean radius appeared to show a small outward acceleration. This scenario is equivalent to a heavy fluid (plasma) accelerating a light fluid (vacuum) and corresponds to an MRT-stable interface. The effects of an accelerating, MRT-stable interface are to introduce an oscillation in the perturbation amplitude; however, the mean instability amplitude growth (before saturation, 260 ns) showed no apparent oscillation, indicating that this type of MRT effect was minimal.

An additional scenario where MRT may develop arises for the kink-seeded liners. As the foil makes minimal contact with the seeded support structure, it may be possible for regions of the foil to implode into the gaps of the support structure and develop MRT in the process. Any MRT growth would complicate the assertion that MRT is decoupled from the kink instability. However, the resulting MRT development is found to be much less important when compared to the deformation of the foil about the seeded structure. The maximum distance the mean foil interface can travel is $s = 0.4$ mm, equal to one half of the seeded support structure amplitude. For a constant acceleration, the MRT gain for a displacement s at the seeded wavelength ($\lambda = 1.27$ mm) is given by $G = \mathrm{Cosh}[\sqrt{2ks}] \sim 4$, where $k = 2\pi/\lambda$ is the instability wavenumber (see Appendix A in Ref. 10). For the foil to have obtained the maximum displacement, it must have completely deformed about the support structure and, therefore, obtained an amplitude of 0.8 mm in the process (equal to the support structure amplitude). For this amplitude to have been generated by MRT alone would require an initial perturbation of $A_0 = 0.2$ mm, which is unreasonable for two reasons: (1) we do not see such a perturbation on the preshot images, which can clearly resolve features exceeding 0.1 mm and (2) when the experimental images were taken

($t > 200$ ns, see Fig. 7(b)), we do not see an instability amplitude of 0.8 mm, but rather of $A_1 \sim 0.2$ mm. On the other hand, let us suppose that the amplitude A_1 at $t \sim 200$ ns was generated by MRT alone. This requires an initial perturbation of $A_0 = 0.05$ mm (for $G = 4$); but again, in order for a displacement of $s = 0.4$ mm have occurred, the foil must have taken the shape of the seeded support structure, and in the process gained an amplitude of 0.8 mm, which is large compared to A_1. We, therefore, conclude that MRT plays little role during any initial implosion of the foil towards the support structure, and that the dominant instability development throughout the discharge is due to the kink instability.

The data in Fig. 7(c) and Table I also show that the plasma radius is slightly smaller when adding an axial magnetic field, while having little effect on the expansion rate. This suggests that the axial magnetic field may be delaying or reducing the plasma expansion early in time during the current pulse when the axial magnetic field is appreciable compared to the azimuthal magnetic field. We note that the mean radius of the ablated seeded liners was smaller than the unseeded; however, this was primarily due to the smaller mean radius of the seeded support structure (5.65 mm) versus the unseeded (6.35 mm).

The azimuthal mode number may be studied for the unseeded, magnetized liner by analyzing the self-emission striations and their relationship to the instability bumps, as shown in Fig. 6. In general, the shadowgraph/self-emission diagnostic showed dark and bright striations connecting instability bumps and necks. However, the bright and dark striations were not as clearly visible for the unseeded, magnetized liner, likely due to the smaller amplitude instability structures, as indicated above. For this reason, the central region of the image in Fig. 6 was contrast-enhanced, which clarified the striations in addition to revealing an asymmetry in self-emission across the face of the plasma, with more light emission from the right side; a possible explanation being asymmetry in current flow due to imperfect contact of the liner support structure with the load hardware. The locations of the dark striations were determined using an algorithm that tracked self-emission minima across the face of the plasma. Pixel values in the image were locally averaged over 15 pixels to avoid tracking small feature noise. Vertical lineouts were taken for each pixel across the face of the plasma, where local minima correspond to dark self-emission regions. The positions of these minima were tracked horizontally across the plasma, as shown in white in Fig. 6. Due to the weak signal, not all of the striations could be tracked completely across the plasma; the top striation, for example, could only be tracked across one fourth of the circumference. The measured striation signal may then be compared to the signal expected from an $m = +2$ mode, shown in black. The black solid lines connect instability bumps on the front side of the plasma, and the dashed line shows the required connection on the back side of the plasma in order that the pitch angle with respect to the horizontal is the same for the front and back side. This procedure yields the $m = +2$ mode. As shown in the figure, the solid black ($m = +2$ projection) and white (measured signal) lines are in an overall agreement. Thus, bump #2 must connect to bump

#5. We therefore interpret the instability as an $m = +2$ helical mode, consisting of two intertwined helices that spiral in the same sense of rotation as the global magnetic field. Supposing that bump #2 connects to bump #3, which would be required for an $m = +1$ mode, is unreasonable because the striation line on the back face would be nearly horizontal, in disagreement with the observed striations on the front face. We emphasize, once more, that while we do not have a simultaneous measurement of self-emission on the back face of the plasma, this identification of the $m = +2$ mode comes from careful consideration (1) that striations connect bump-to-bump features on the back face of the plasma and (2) that the angles of the measured striations on the front side of the plasma are similar to those on the back side.

The results of the unseeded liner experiments highlight two important effects of axial magnetic fields (Figs. 5(a) and 5(b)). First, the azimuthal symmetry was destroyed and a helically oriented instability structure arose, spiraling in the direction of the global magnetic field spiral. Second, the overall instability amplitude was reduced; however, the growth rate was not significantly affected when the wavelengths were similar, from 250 to 290 ns (Fig. 7(a)). This indicates that the axial magnetic field played an important role in determining the instability mode early in time when its value was relatively large compared to the azimuthal field but had little effect later in time on the growth rate of the structures when the azimuthal field dominated the axial field.

The observation that the axial magnetic field resulted in an $m = +2$ helical mode (cf. Figs. 5(b) and 6) made it difficult to isolate the stabilizing effects of an axial magnetic field for a given mode, as larger axial fields could induce higher m modes. This motivated the design of the $|m| = 1$ kink-seeded support structure. In this manner, the same azimuthal mode and axial wavelength could be generated in order to directly compare the effects of axial magnetic fields. However, directly comparing the seeded instability growth rate to the unseeded growth may not be straightforward, as the structures may have an additional growth mechanism that is not due to the kink instability. For example, the helical support structure may be ablating at the thin edges of the screw threads and therefore contributing more plasma to the bumps than the necks. This was not likely the case for the smoother, unseeded liners where any support structure ablation is expected to be much more uniform. An improved seeded support structure could soften the threaded edges in order to test the effects of ablation.

The results of the seeded experiments highlight the importance of the direction of the axial magnetic field for a given kink mode. When the helix spiraled in the direction of the global magnetic field spiral ($m = +1$, Fig. 5(d)), the instability amplitude was reduced early in time but reached the same amplitude as the unmagnetized liner by 270 ns, indicating the importance of the axial field early in time and its unimportance later in time (Fig. 7(b)). During this time, the growth rate was *larger* relative to the unmagnetized case, which may be understood by the following two effects: first, the axial magnetic field effects were reduced later in time as the azimuthal field peaked, and second, the growth rate was larger because the ratio of the amplitude to the wavelength

was initially smaller than that of the unmagnetized case, indicating that the growth rate was better described by the linear perturbation theory (characterized by exponential growth in time). Inverting the direction of the axial magnetic field while maintaining the same direction of the seeded helix produced an $m = -1$ mode and demonstrated an overall mitigation of instability development (Fig. 5(e)). This dramatic difference is expected, as the helical structure was seeded with $m = -1$. This result demonstrates the importance of the sign of the helical mode; negative m modes are more stable because they require more energy to bend magnetic field lines. In addition, the seeded, $+1.6$ T magnetized liner showed an overall *decrease* in amplitude starting around 250 ns (cf. Fig. 7(b)). One possible explanation is that as the outer surface obtains a small outward acceleration, the plasma-vacuum interface becomes an MRT stable interface, reducing (and perhaps completely stabilizing) the kink instability growth. This may have also occurred for the other seeded liners tested, which showed a reduction in amplitude when there is an outward acceleration in the mean radius (Fig. 7(c)). While the true interface acceleration is difficult to measure due to the small changes in radius, additional studies of the late-time behavior could help validate this explanation.

B. Analytic growth rate calculations using Weis-Zhang theory for experimental parameters

In order to study the development of helical modes, we used the Weis-Zhang theory[9,10] to calculate the instantaneous theoretical sausage and helical growth rates using parameters determined from the experiment, including the time-dependent azimuthal magnetic field. While the instabilities appear to have developed beyond the direct applicability of the linear perturbation theory, we may still use the Weis-Zhang theory to (1) gain insight into the instability development that occurred earlier in time but was not imaged and (2) isolate the stabilizing effects of axial magnetic fields for various azimuthal mode numbers, while fixing the remaining parameters (azimuthal magnetic field, plasma thickness, density, radius, and instability axial wavelength) with reasonable values from the experiment. The two parameters that were estimated and not directly measured were the liner thickness and plasma density; however, these parameters primarily affect the numerical scaling of the growth rate curve. Reasonable values for these parameters were chosen as follows. The plasma thickness may be estimated from the difference between the plasma and support structure radius, which ranges from 0.6 to 1.3 mm. As the growth rates are extremely insensitive to liner thicknesses exceeding 0.2 mm, we set the thickness to 0.5 mm to characterize possible thicknesses between 0.2 and 1.3 mm. For the plasma density, similar experiments on MAIZE using the same foils measured an electron density of $n_e \sim 10^{19}/\text{cm}^3$ at the edge of the plasma using interferometry.[18] A second estimate for the plasma density may be determined by assuming the dark shadowgraph band is due to laser cutoff at the critical density ($\sim 4 \times 10^{21}/\text{cm}^3$). Therefore, a reasonable density characterizing this range is $n \sim 10^{20}/\text{cm}^3$, corresponding to a mass density of $\rho = 4.5 \text{ kg/m}^3$. Despite the uncertainty in the density

estimate, a change in density will primarily affect the numerical values of the growth rate. For example, due to the $\sim 1/\rho^{1/2}$ scaling of growth rate with density (see Ref. 10), an increase in density in the curves below would primarily decrease the numerical values while negligibly changing the temporal profile.

In Fig. 8(a), we plotted the growth rate for $|m| = 0$, 1, and 2 modes with and without an axial magnetic field of $+1.1$ T, corresponding to the unseeded liner experiments. These calculations were performed for 250 ns (time of peak current) for a small wavelength of 0.3 mm, which is roughly the wavelength of the first detectable instability structures found in similar liner experiments,[16] presumably generated by electrothermal instability. For these plots, recall that a

positive m mode indicates a helix with spiral direction in the same sense as the global magnetic field spiral. We found that the axial magnetic field completely stabilized the small wavelength modes until 70 ns, at which point the $m = +2$ mode became the first to destabilize, followed by the $m = +1$, $m = 0$, and finally, $m = -1$ modes. Beyond this point, the growth rates were similar, with a slight preference to the $m = +2$ mode, indicating that this mode should dominate, as found in the experiment. With no axial magnetic field, the $m = 0$ and $m = 1$ modes had almost identical growth rates, with a slight preference to the sausage mode, $m = 0$. The dominance of the $m = 0$ instability, despite the similarity in theoretical growth rates, indicates that there may be a seeding mechanism for the sausage mode that occurs early on in the discharge; one such candidate is the electrothermal instability.[19]

In Fig. 8(b), we compare the growth rate of the $m = +1$ kink instability for axial fields of 0 T and 1.6 T using the longer wavelength of 1.27 mm. These parameters correspond to the experimental values for the seeded liners. This plot shows that the $m = -1$ mode is completely stabilized for 70 ns, and after this point has a reduced growth rate for the remainder of the pulse. The $m = +1$ mode is stabilized for a shorter period of time (50 ns), after which its growth quickly approaches the unmagnetized case. These calculations are consistent with the experimental observations: the $m = -1$ seeded liner showed the most stable structures, while the $m = +1$ seeded liner showed initially smaller structures that grew to amplitudes comparable of those in the $m = 1$ unmagnetized liner.

We did not directly compare the experimental growth rate to the theory for two reasons. First, the exhibited growth was generally algebraic, which indicated these structures had evolved beyond the direct applicability of the linear perturbation theory. In other words, the ratio of amplitude to wavelength was not small, and nonlinear effects must be accounted for. Second, the growth rates require knowledge of the plasma thickness, and more importantly density, which were not measured in the experiment. Despite these limitations, the analytic growth rates are useful tools for revealing the possible dominant modes expected for a given axial magnetic field at a fixed set of parameters. As noted above, changing the density will not change which modes are stabilized early in time, nor the relative scaling of modes for a given axial magnetic field.
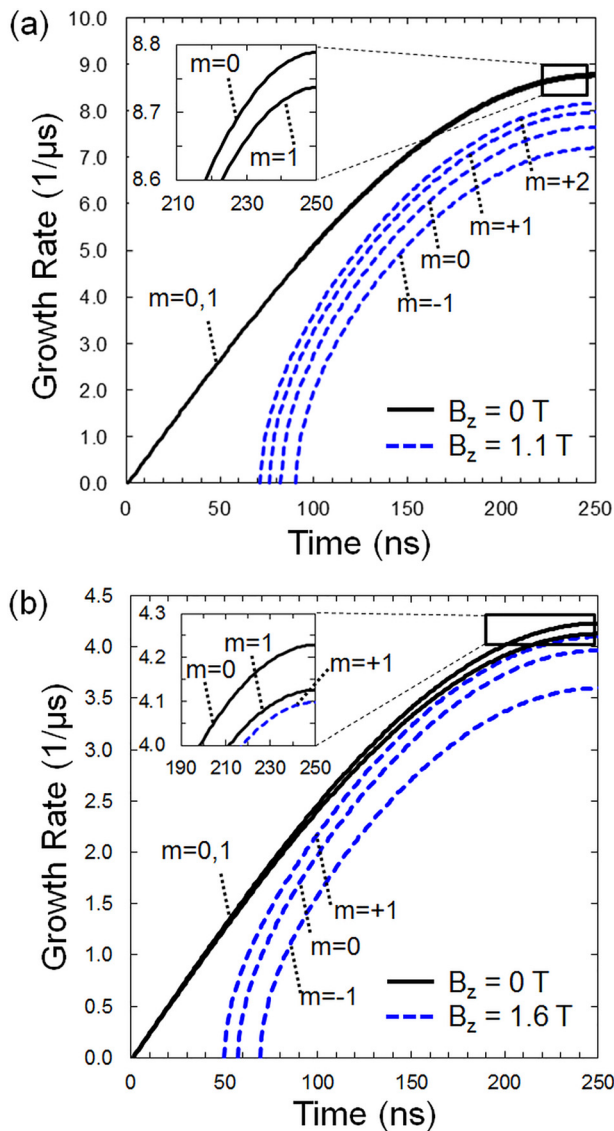
FIG. 8. Analytic calculations for sausage and helical growth rates using the Weis-Zhang theory for: (a) small wavelength (0.3 mm) and (b) kink-seeded wavelength (1.27 mm). Growth rates are limited to linear perturbation theory and were calculated using known time-dependent experimental parameters (magnetic fields) and estimated parameters (liner thickness and density, estimated to be 500 μm and 4.5 kg/m^3). The growth rate is insensitive to thickness and scales with density as $\sim 1/\rho^{1/2}$ so that a variation in these parameters will only change the amplitude and not the shape of the curves. To exclude coupling effects to MRT, these calculations did not include liner acceleration.

VI. CONCLUSION

In this paper, we have studied sausage and helical modes in cylindrical liner-plasmas in order to determine the effects of axial magnetic fields using 12-frame laser shadowgraphy and visible self-emission. Dark and bright striation lines in self-emission enabled the instability structures to be connected from left and right sides of the plasma for individual shots in order to identify the azimuthal mode number. The plasma acceleration was minimized by employing an inner plastic support structure in order to prevent implosion and therefore minimize the effects of MRT. Unseeded, unmagnetized liners developed an $m = 0$ sausage instability that grew

in amplitude throughout the discharge. Adding an axial magnetic field resulted in an $m = +2$ helical mode spiraling in the $-\mathbf{z}$ direction, corresponding to the spiral direction of the global magnetic field. These structures showed a reduction in overall instability amplitude and growth rate and saturated in growth at 330 ns. The $|m| = 1$ kink mode was seeded by modifying the inner support structure using a plastic threaded rod spiraling in the $+\mathbf{z}$ direction and showed large amplitude structures that saturated in growth at 260 ns. Adding an axial magnetic field in the $-\mathbf{z}$ direction showed initially smaller amplitude structures that grew with a faster growth rate to the same amplitude of the unmagnetized, seeded liners, whereas inverting the axial field resulted in significant stabilizing effects throughout the duration of the discharge.

In order to study the effects of axial magnetic field on instability development, the time-dependent theoretical growth rates for sausage and helical modes were calculated using the Weis-Zhang perturbation theory for an ideal MHD cylindrical liner, using estimated parameters from the experiment. It was found that early in the current pulse, there is a window in time when sausage modes are completely stabilized, while the helical modes are not. In addition, for a seeded kink mode, the calculations show that in the presence of an axial magnetic field, the sign of m plays an important role in determining the instability onset time and growth rate, with $(-m)$ modes being much more stable than $(+m)$ modes.

The onset of the $m = +2$ helical mode, which we carefully identified, due to a relatively small axial magnetic field was a surprising result. It motivates further study of the dependency of the azimuthal mode number on the initial, external axial magnetic field value. In fact, one open problem is to determine the minimum axial magnetic field required to disrupt the azimuthal symmetry observed in the unmagnetized case. These problems shall be left for future work.

ACKNOWLEDGMENTS

[1] R. B. Spielman, D. L. Hanson, M. A. Palmer, M. K. Matzen, T. W. Hussey, and J. M. Peek, J. Appl. Phys. **57**, 830 (1985).

[2] C. A. Coverdale, C. Deeney, A. L. Velikovich, R. W. Clark, Y. K. Chong, J. Davis, and J. Franklin, Phys. Plasmas **14**, 022706 (2007).

[3] T. W. L. Sanford, G. O. Allshouse, B. M. Marder, T. J. Nash, R. C. Mock, R. B. Spielman, and M. Vargas, Phys. Rev. Lett. **77**, 5063 (1996).

[4] R. B. Spielman, C. Deeney, G. A. Chandler, M. R. Douglas, D. L. Fehl, M. K. Matzen, and J. F. Seamen, Phys. Plasmas **5**, 2105 (1998).

[5] M. K. Matzen, Phys. Plasmas **4**, 1519 (1997).

[6] R. C. Kirkpatrick, I. R. Lindemuth, and M. S. Ward, Fusion Sci. Technol. **27**, 201 (1995).

[7] T. Intrator, S. Y. Zhang, J. H. Degnan, I. Furno, C. Grabowski, S. C. Hsu, and W. J. Waganaar, Phys. Plasmas **11**, 2580 (2004).

[8] M. R. Gomez, S. A. Slutz, A. B. Sefkow, K. D. Hahn, S. B. Hansen, P. F. Knapp, and C. A. Jennings, Phys. Plasmas **22**, 056306 (2015).

[9] M. R. Weis, P. Zhang, Y. Y. Lau, P. F. Schmit, K. J. Peterson, M. Hess, and R. M. Gilgenbach, Phys. Plasmas **22**, 032706 (2015).

[10] M. R. Weis, Ph.D. thesis, University of Michigan, Ann Arbor, 2015.

[11] R. D. McBride, M. R. Martin, R. W. Lemke, J. B. Greenly, C. A. Jennings, D. C. Rovang, D. B. Sinars, M. E. Cuneo, M. C. Herrmann, S. A. Slutz, C. W. Nakhleh, D. D. Ryutov, J.-P. Davis, D. G. Flicker, B. E. Blue, K. Tomlinson, D. Schroen, R. M. Stamm, G. E. Smith, J. K. Moore, T. J. Rogers, G. K. Robertson, R. J. Kamm, I. C. Smith, M. Savage, W. A. Stygar, G. A. Rochau, M. Jones, M. R. Lopez, J. L. Porter, and M. K. Matzen, Phys. Plasmas **20**, 056309 (2013).

[12] T. J. Awe, C. A. Jennings, R. D. McBride, M. E. Cuneo, D. C. Lamppa, M. R. Martin, D. C. Rovang, D. B. Sinars, S. A. Slutz, A. C. Owen, K. Tomlinson, M. R. Gomez, S. B. Hansen, M. C. Herrmann, M. C. Jones, J. L. McKenney, G. K. Robertson, G. A. Rochau, M. E. Savage, D. G. Schroen, and W. A. Stygar, Phys. Plasmas **21**, 056303 (2014).

[13] J. C. Valenzuela, G. W. Collins IV, D. Mariscal, E. S. Wyndham, and F. N. Beg, Phys. Plasmas **21**, 031208 (2014).

[14] L. Atoyan, D. A. Hammer, B. R. Kusse, T. Byvank, A. D. Cahill, J. B. Greenly, S. A. Pikuz, and T. A. Shelkovenko, Phys. Plasmas **23**, 022708 (2016).

[15] R. M. Gilgenbach, M. R. Gomez, J. C. Zier, W. W. Tang, D. M. French, Y. Y. Lau, M. G. Mazarakis, M. E. Cuneo, M. D. Johnston, B. V. Oliver, T. A. Mehlhorn, A. A. Kim, and V. A. Sinebryukhov, AIP Conf. Proc. **1088**, 259 (2009).

[16] D. A. Yager-Elorriaga, A. M. Steiner, S. G. Patel, N. M. Jordan, Y. Y. Lau, and R. M. Gilgenbach, Rev. Sci. Instrum. **86**, 113506 (2015).

[17] D. C. Rovang, D. C. Lamppa, M. E. Cuneo, A. C. Owen, J. McKenney, D. W. Johnson, S. Radovich, R. J. Kaye, R. D. McBride, C. S. Alexander, T. J. Awe, S. A. Slutz, A. B. Sefkow, T. A. Haill, P. A. Jones, J. W. Argo, D. G. Dalton, G. K. Robertson, E. M. Waisman, D. B. Sinars, J. Meissner, M. Milhous, D. N. Nguyen, and C. H. Mielke, Rev. Sci. Instrum. **85**, 124701 (2014).

[18] D. A. Yager-Elorriaga, N. M. Jordan, S. G. Patel, A. M. Steiner, Y. Y. Lau, and R. M. Gilgenbach, oral presentation at the International Conference on Plasma Science, Antalya, Turkey, 24–28 May 2015.

[19] K. J. Peterson, D. B. Sinars, E. P. Yu, M. C. Herrmann, M. E. Cuneo, S. A. Slutz, I. C. Smith, B. W. Atherton, M. D. Knudson, and C. Nakhleh, Phys. Plasmas **19**, 092701 (2012).